Super-resolution photon-efficient imaging by nanometric double-helix point spread function localization of emitters (SPINDLE)

Ginni Grover,[1,*] Keith DeLuca,[2] Sean Quirin,[1] Jennifer DeLuca,[2] and Rafael Piestun[1]

[1]*Department of Electrical, Computer and Energy Engineering, University of Colorado, Boulder, Colorado, 80309, USA*

[2] *Department of Biochemistry and Molecular Biology, Colorado State University, Fort Collins, Colorado, 80523, USA*

[*]*Ginni.Grover@colorado.edu*

Abstract: Super-resolution imaging with photo-activatable or photo-switchable probes is a promising tool in biological applications to reveal previously unresolved intra-cellular details with visible light. This field benefits from developments in the areas of molecular probes, optical systems, and computational post-processing of the data. The joint design of optics and reconstruction processes using double-helix point spread functions (DH-PSF) provides high resolution three-dimensional (3D) imaging over a long depth-of-field. We demonstrate for the first time a method integrating a Fisher information efficient DH-PSF design, a surface relief optical phase mask, and an optimal 3D localization estimator. 3D super-resolution imaging using photo-switchable dyes reveals the 3D microtubule network in mammalian cells with localization precision approaching the information theoretical limit over a depth of 1.2 μm.

OCIS codes: (180.6900) Three-dimensional microscopy; (180.2520) Fluorescence microscopy; (050.4865) Optical vortices; (110.4850) Optical transfer functions; (110.1758) Computational imaging; (170.3880) Medical and biological imaging.

References and Links

1. E. Abbe, "Contributions to the theory of the microscope and microscopic observations (translated from German)," Archiv für Mikroskopische Anatomie **9**, 413–468 (1873).
2. L. Schermelleh, P. M. Carlton, S. Haase, L. Shao, L. Winoto, P. Kner, B. Burke, M. C. Cardoso, D. A. Agard, M. G. L. Gustafsson, H. Leonhardt, and J. W. Sedat, "Subdiffraction multicolor imaging of the nuclear periphery with 3D structured illumination microscopy," Science **320**(5881), 1332–1336 (2008).
3. R. Schmidt, C. A. Wurm, S. Jakobs, J. Engelhardt, A. Egner, and S. W. Hell, "Spherical nanosized focal spot unravels the interior of cells," Nat. Methods **5**(6), 539–544 (2008).
4. E. Betzig, G. H. Patterson, R. Sougrat, O. W. Lindwasser, S. Olenych, J. S. Bonifacino, M. W. Davidson, J. Lippincott-Schwartz, and H. F. Hess, "Imaging intracellular fluorescent proteins at nanometer resolution," Science **313**(5793), 1642–1645 (2006).
5. S. T. Hess, T. P. K. Girirajan, and M. D. Mason, "Ultra-high resolution imaging by fluorescence photoactivation localization microscopy," Biophys. J. **91**(11), 4258–4272 (2006).
6. M. J. Rust, M. Bates, and X. Zhuang, "Sub-diffraction-limit imaging by stochastic optical reconstruction microscopy (STORM)," Nat. Methods **3**(10), 793–796 (2006).
7. M. Heilemann, S. van de Linde, M. Schüttpelz, R. Kasper, B. Seefeldt, A. Mukherjee, P. Tinnefeld, and M. Sauer, "Subdiffraction-resolution fluorescence imaging with conventional fluorescent probes," Angew. Chem. Int. Ed. Engl. **47**(33), 6172–6176 (2008).
8. J. Fölling, M. Bossi, H. Bock, R. Medda, C. A. Wurm, B. Hein, S. Jakobs, C. Eggeling, and S. W. Hell, "Fluorescence nanoscopy by ground-state depletion and single-molecule return," Nat. Methods **5**(11), 943–945 (2008).
9. B. Huang, W. Wang, M. Bates, and X. Zhuang, "Three-dimensional super-resolution imaging by stochastic optical reconstruction microscopy," Science **319**(5864), 810–813 (2008).
10. M. F. Juette, T. J. Gould, M. D. Lessard, M. J. Mlodzianoski, B. S. Nagpure, B. T. Bennett, S. T. Hess, and J. Bewersdorf, "Three-dimensional sub-100 nm resolution fluorescence microscopy of thick samples," Nat. Methods **5**(6), 527–529 (2008).

#173795 - $15.00 USD Received 6 Aug 2012; revised 16 Oct 2012; accepted 5 Nov 2012; published 12 Nov 2012

11. G. Shtengel, J. A. Galbraith, C. G. Galbraith, J. Lippincott-Schwartz, J. M. Gillette, S. Manley, R. Sougrat, C. M. Waterman, P. Kanchanawong, M. W. Davidson, R. D. Fetter, and H. F. Hess, "Interferometric fluorescent super-resolution microscopy resolves 3D cellular ultrastructure," Proc. Natl. Acad. Sci. U.S.A. **106**(9), 3125–3130 (2009).
12. S. R. P. Pavani, M. A. Thompson, J. S. Biteen, S. J. Lord, N. Liu, R. J. Twieg, R. Piestun, and W. E. Moerner, "Three-dimensional, single-molecule fluorescence imaging beyond the diffraction limit by using a double-helix point spread function," Proc. Natl. Acad. Sci. U.S.A. **106**(9), 2995–2999 (2009).
13. J. Tang, J. Akerboom, A. Vaziri, L. L. Looger, and C. V. Shank, "Near-isotropic 3D optical nanoscopy with photon-limited chromophores," Proc. Natl. Acad. Sci. U.S.A. **107**(22), 10068–10073 (2010).
14. D. Baddeley, M. B. Cannell, and C. Soeller, "Three-dimensional sub-100 nm super-resolution imaging of biological samples using a phase ramp in the objective pupil," Nano Research **4**(6), 589–598 (2011).
15. D. Aquino, A. Schönle, C. Geisler, C. V. Middendorff, C. A. Wurm, Y. Okamura, T. Lang, S. W. Hell, and A. Egner, "Two-color nanoscopy of three-dimensional volumes by 4Pi detection of stochastically switched fluorophores," Nat. Methods **8**(4), 353–359 (2011).
16. S. A. Jones, S.-H. Shim, J. He, and X. Zhuang, "Fast, three-dimensional super-resolution imaging of live cells," Nat. Methods **8**(6), 499–505 (2011).
17. F. Cella Zanacchi, Z. Lavagnino, M. Perrone Donnorso, A. Del Bue, L. Furia, M. Faretta, and A. Diaspro, "Live-cell 3D super-resolution imaging in thick biological samples," Nat. Methods **8**(12), 1047–1049 (2011).
18. G. Grover, S. R. P. Pavani, and R. Piestun, "Performance limits on three-dimensional particle localization in photon-limited microscopy," Opt. Lett. **35**(19), 3306–3308 (2010).
19. R. Piestun and J. Shamir, "Synthesis of three-dimensional light fields and applications," Proc. IEEE **90**(2), 222–244 (2002).
20. S. Quirin, S. R. P. Pavani, and R. Piestun, "Optimal 3D single-molecule localization for superresolution microscopy with aberrations and engineered point spread functions," Proc. Natl. Acad. Sci. U.S.A. **109**(3), 675–679 (2012).
21. S. R. P. Pavani and R. Piestun, "High-efficiency rotating point spread functions," Opt. Express **16**(5), 3484–3489 (2008).
22. S. R. P. Pavani and R. Piestun, "Three dimensional tracking of fluorescent microparticles using a photon-limited double-helix response system," Opt. Express **16**(26), 22048–22057 (2008).
23. M. A. Thompson, M. D. Lew, M. Badieirostami, and W. E. Moerner, "Localizing and tracking single nanoscale emitters in three dimensions with high spatiotemporal resolution using a double-helix point spread function," Nano Lett. **10**(1), 211–218 (2010).
24. M. A. Thompson, J. M. Casolari, M. Badieirostami, P. O. Brown, and W. E. Moerner, "Three-dimensional tracking of single mRNA particles in Saccharomyces cerevisiae using a double-helix point spread function," Proc. Natl. Acad. Sci. U.S.A. **107**(42), 17864–17871 (2010).
25. A. Greengard, Y. Y. Schechner, and R. Piestun, "Depth from diffracted rotation," Opt. Lett. **31**(2), 181–183 (2006).
26. D. B. Conkey, R. P. Trivedi, S. R. P. Pavani, I. I. Smalyukh, and R. Piestun, "Three-dimensional parallel particle manipulation and tracking by integrating holographic optical tweezers and engineered point spread functions," Opt. Express **19**(5), 3835–3842 (2011).
27. S. Ram, J. Chao, P. Prabhat, E. S. Ward, and R. J. Ober, "A novel approach to determining the three-dimensional location of microscopic objects with applications to 3D particle tracking," Proc. SPIE 64430D, 64430D-7 (2007).
28. Y. Y. Schechner, R. Piestun, and J. Shamir, "Wave propagation with rotating intensity distributions," Phys. Rev. E Stat. Phys. Plasmas Fluids Relat. Interdiscip. Topics **54**(1), R50–R53 (1996).
29. G. Indebetouw, "Optical Vortices and Their Propagation," J. Mod. Opt. **40**(1), 73–87 (1993).
30. G. Grover, S. Quirin, C. Fiedler, and R. Piestun, "Photon efficient double-helix PSF microscopy with application to 3D photo-activation localization imaging," Biomed. Opt. Express **2**(11), 3010–3020 (2011).
31. S. Wolter, M. Schüttpelz, M. Tscherepanow, S. VAN DE Linde, M. Heilemann, and M. Sauer, "Real-time computation of subdiffraction-resolution fluorescence images," J. Microsc. **237**(1), 12–22 (2010).
32. A. Neubeck and L. Van Gool, "Efficient non-maximum suppression," in *Proceedings of 18th International Conference on Pattern Recognition* (IEEE Computer Society, 2006) pp. 850–855.
33. A. Egner and S. W. Hell, "Aberrations in Confocal and Multi-Photon Fluorescence Microscopy Induced by Refractive Index Mismatch," in *Handbook of Biological Confocal Microscopy*, J. B. Pawley ed., Third Ed. (Springer Science, New York, 2003), pp. 404–413, Chap. 20.
34. M. Bates, B. Huang, G. T. Dempsey, and X. Zhuang, "Multicolor super-resolution imaging with photo-switchable fluorescent probes," Science **317**(5845), 1749–1753 (2007).
35. J. F. Kenney and E. S. Keeping, "The distribution of the standard deviation," in *Mathematics of Statistics* 2nd ed. (Van Nostrand, 1951), Vol. Part 2, pp. 170–173.
36. L. Novotny and B. Hecht, "Chapter 4," in *Principles of Nano-Optics* (Cambridge University Press, 2006).
37. M. Newberry, "CCD camera gain measurement," http://www.mirametrics.com/tech_note_ccdgain.htm.
38. M. H. Ulbrich and E. Y. Isacoff, "Subunit counting in membrane-bound proteins," Nat. Methods **4**(4), 319–321 (2007).
39. K. I. Mortensen, L. S. Churchman, J. A. Spudich, and H. Flyvbjerg, "Optimized localization analysis for single-molecule tracking and super-resolution microscopy," Nat. Methods **7**(5), 377–381 (2010).

#173795 - $15.00 USD Received 6 Aug 2012; revised 16 Oct 2012; accepted 5 Nov 2012; published 12 Nov 2012

40. S. R. P. Pavani, A. Greengard, and R. Piestun, "Three-dimensional localization with nanometer accuracy using a detector-limited double-helix point spread function system," Appl. Phys. Lett. **95**(2), 021103 (2009).

1. Introduction

Optical diffraction limits the resolution in the visible spectrum to about 200 nm in the transverse direction and 500 nm in depth [1]. Therefore observation of cellular structures which are of the order of tens of nanometer is not possible with traditional optical microscopy. As an alternative, biologists have relied on electron and x-ray microscopy to image such small structures. However, these techniques are damaging to the sample and preclude live-cell imaging. Recently, simultaneous advances in optical methods and engineering of the fluorescent properties of dyes and proteins have enabled tools that overcome the optical diffraction barrier and facilitate imaging at the nanometer scale. Several methods have been developed to overcome the diffraction limit in three dimensions. One approach is to engineer the excitation pattern using structured illumination [2] or scanning localized beams as in stimulated emission depletion microscopy [3]. Another super-resolution approach involves stochastically activating sparse sets of emitters distributed within the field of view which are sequentially changed over time. This time-sequential imaging provides a map of particle localizations that generates a 2D or 3D super-resolution image. Different mechanisms for the control of the emission lend different names to the technique including (fluorescence) photoactivated localization microscopy (PALM) [4,5], (direct) stochastic optical reconstruction microscopy (STORM) [6,7], and ground state depletion microscopy followed by individual molecule return (GSDIM) [8]. These super-resolution approaches have been extended to three dimensions by using microscope modalities that modify the optical point spread function to extract 3D information from the imaged emitters. Resolution below 50 nm in the transverse direction and 100 nm in depth are now possible. 3D microscopes with astigmatic response [9], bi-plane detection [10], interferometric detection (IPALM) [11], double-helix point spread function (DH-PSF) [12], tilted mirrors [13] and phase ramps [14] have been applied to super-resolution imaging.

While 3D PALM/STORM methods enable scanning-free volume imaging, the depth range depends upon the technique. Typical values, using high numerical aperture objective lenses, are 650 nm for the interferometric method [15], 800 nm for the astigmatic method [9], 1000 nm for the bi-plane method [10], and 2000 nm for the DH-PSF [12]. The DH-PSF provides the longest depth range making it attractive to image cells with minimal focus scanning. The astigmatic PSF method has recently been extended to imaging depths from 10 μm to 150 μm enabling whole-cell and live-cell imaging with focus scanning and additional use of optical techniques such as light sheet illumination [16,17].

Biological super-resolution imaging would benefit from the development of optical systems that provide control of the transverse spread of the PSF and depth range [18]. The PSF spread determines the localization precision in the presence of noise as well as the allowed active molecule density per image acquisition. For instance, if a specimen is 500 nm deep, the use of a PSF design with 2000 nm range would not be optimal because it would unnecessarily compromise the signal to noise ratio. This is in turn the result of a fundamental tradeoff between PSF depth range and PSF spread [18,19]. Furthermore, the implementation of the PSF should not degrade the photon collection efficiency and hence the use of highly transmissive phase masks to generate application specific PSFs is critical [30]. The estimation and reconstruction algorithms are also essential to take advantage of the information delivered by the photon limited molecular images [20].

Therefore, in this letter we start by presenting for the first time a general methodology for double-helical PSF mask design based on an analytic expression, which can be adapted to specific imaging and sensing tasks. The analytic approach contributes to a better understanding of the wave optical physical processes involved in helical PSFs. By reducing the DH-PSF design to the determination of a few parameters, we gain insight into the

#173795 - $15.00 USD Received 6 Aug 2012; revised 16 Oct 2012; accepted 5 Nov 2012; published 12 Nov 2012

performance tradeoffs and possibilities of PSF engineering. Similar to other passive optical elements such as gratings and lenses, helical PSF masks are now described by a few parameters as a result of this new approach.

We subsequently introduce a 3D nanoscopic system based on a Fisher information optimized DH-PSF design, a surface relief phase mask implementation for efficient light collection, and a matched optimal reconstruction algorithm for efficient estimation and image reconstruction. The new DH-PSF improves the Fisher information for 3D localization thereby increasing the fundamental precision over previous designs. These characteristics significantly advance earlier implementations of DH-PSF localization microscopy, and involve major innovations in PSF design, mask fabrication, statistical signal processing, as well as overall system integration with respect to earlier DH-PSF implementations [12]. Hence the new integrated methodology is termed Super-resolution Photon-efficient Imaging by Nanometric DH-PSF Localization of Emitters (or SPINDLE).

Finally, SPINDLE experiments reveal 3D super-resolution imaging of microtubules in mammalian cells (Rat-Kangaroo Epithelial cells) with single-molecule sensitivity over the longest depth range demonstrated so far without focus scanning. The average experimental molecule localization precision (with ~30 background photons) is $(\sigma_x, \sigma_y, \sigma_z) = (2.5, 3.8, 16.5)$ nm with 6000 collected photons and $(\sigma_x, \sigma_y, \sigma_z) = (22, 29, 52)$ nm with 1100 photons. We further show that these numbers are very close to the theoretical precision limits.

2. An information optimized DH-PSF design

A DH-PSF is an engineered PSF which displays two lobes in the transverse plane that rotate with defocus [21]. Thus, the PSF forms a double-helix of light in 3D space for each and every point-like source. The advantage of this PSF is that the axial position of the imaged point source is encoded in the rotation of the two lobes. The pupil plane phase mask and the transverse slices of the DH-PSF for various defocus positions of a high NA microscope are shown in Figs. 1(a) and 1(b), respectively. The DH-PSF enhances the Fisher information for axial localization and can be used for 3D imaging applications like localization based microscopy [22], particle tracking [22–24], super-resolution imaging [12], depth ranging [25], profilometry and imaging optical tweezers [26]. The DH-PSF allows 3D localization of multiple sparse particles in a single image with high localization precision and longer depth-of-field than other 3D localization methods [18], making it attractive for tracking and super-resolution imaging.

In localization microscopy applications there is always some level of unavoidable background noise, which affects the localization precision and the system resolution. To illustrate this, a comparison of the 3D localization precision limits from three alternative optical PSF choices is shown in Fig. 1(e). The fundamental localization precision of a system is determined by the PSF, the number of photons detected, the numerical aperture, and noise; along with other practical parameters such as PSF sampling. This fundamental limit is defined by the Cramer-Rao lower bound (CRB), which is the best achievable precision by any unbiased estimator, $\sigma_{estimator} \geq \sqrt{CRB}$ [18,22,27]. For transverse shift-invariant and axial shift-variant systems, the CRB associated with localization along each of the three dimensions is a function of the axial position z. The CRB for 3D localization is defined as the arithmetic mean $CRB_{3D}(z) = \frac{1}{3}\left(CRB_X(z) + CRB_Y(z) + CRB_Z(z)\right)$ [18]. This metric is useful because it takes into account the isotropy of the PSF performance. In order to establish the precision performance of the system over a volume, we define the $Avg\left(CRB_{3D}\right)$, which provides the average achievable precision over a given range. In Fig. 1(e), the $Avg\left(CRB_{3D}\right)$ for three systems – astigmatic [9], bi-plane [10], and DH-PSF [21], (labeled respectively as Astig, BP and DH-1 in the figure) are respectively shown for 1 μm imaging depth range, for standard experiment parameters and shot noise model. The original DH-PSF [21] design has been

#173795 - $15.00 USD Received 6 Aug 2012; revised 16 Oct 2012; accepted 5 Nov 2012; published 12 Nov 2012

widely used in microscopy and is hereafter referred to as DH-PSF-1. In this comparison all common parameters are equal while the astigmatic system has 400 nm separation between the two transverse foci and the bi-plane method has 500 nm separation between the two focal planes [10]. The CRB values are plotted as a function of the number of background photons. We notice that for a system with low background, the DH-PSF-1 performs better than the other two methods. The main strength of DH-PSF lies in the long depth-of-field [20]. However, from the CRB calculations we notice that as the background is increased, the DH-PSF-1 performance degrades. This is because the energy in DH-PSF-1 is transversely spread relative to a diffraction limited spot. Hence, the signal to background per pixel decreases faster for the DH-PSF-1 system with increasing background, degrading the achievable precision. Similarly, the bi-plane system spreads out the PSF energy with defocus leading to a lower signal to background and decreasing precision. The astigmatic system, owing to its relatively smaller spread in the transverse plane, behaves better in the presence of high background. However in Ref [18]. it was shown that, by numerical design, it is possible to improve the performance of DH-PSF systems with respect to information theoretic measures. Here we present an analytic design method where the PSF performance is improved in terms of the information theoretic CRB with background noise, leading to improved precision as compared to other methods.

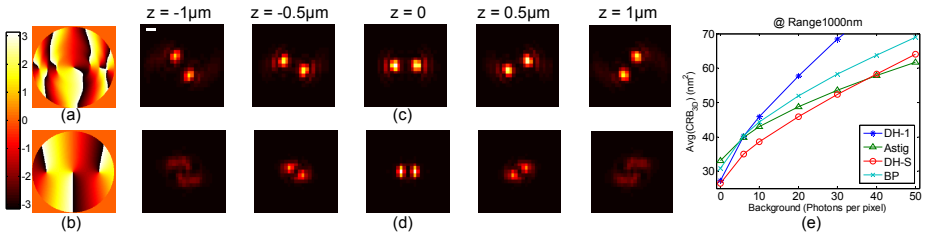

Fig. 1. SPINDLE PSF design with background noise. (a) and (b) are two DH-PSF (DH-1 and DH-S) pupil plane phase masks. (c) and (d) are cross-sections of two PSF designs (DH-1 and DH-S) optimized for different depth ranges and background noise. From left to right the images show the simulated PSF at various defocus positions for a 1.45NA microscope and λ = 660 nm. The scale bar is 500 nm. (e) Comparison of 3D localization methods via the Average Cramer Rao Bound (CRB_{3D}) over 1 µm range with changing background. The calculation parameters for shot-noise limited CRB are 1.45NA 100X system, λ = 660 nm, pixel size = 16 µm, 3000 detected photons at focus. No readout noise is assumed.

Previous phase-only mask designs to generate a DH-PSF have relied on numerical optimization starting with an initial amplitude/phase mask generated by superposition of Gauss-Laguerre modes [18,21]. In contrast, here we generate the DH-PSF analytically as a superposition of vortex singularities in the pupil plane while the optimization is reduced to finding the number of vortices and their relative locations to achieve the desired characteristics (see also Sec. 2.1). To select the best DH-PSF for localization based super-resolution in the presence of background noise, we minimize the average CRB_{3D} for a range exceeding 1µm. The resulting DH-PSF is specifically used for SPINDLE experiments so it is henceforth referred to as DH-PSF-S. The phase mask function is shown in Fig. 1(b) and the transverse cross-sections of the corresponding PSF for different defocus positions are shown in Fig. 1(d).

Figure 1(e) compares the average CRB_{3D} of the DH-PSF-S (labeled as DH-S) with prior designs. The new DH-PSF-S not only provides the best precision for 3D localization experiments with high background but is also more confined transversely as shown in Fig. 1(d). This is advantageous for super-resolution because more particles per image can be detected. For super-resolution PALM/STORM experiments, the PSF confinement translates into faster data acquisition. Note that for experiments with backgrounds up to about 40 photons/pixel, the DH-PSF-S is best for 3D localization. Further, for different depth ranges

#173795 - $15.00 USD Received 6 Aug 2012; revised 16 Oct 2012; accepted 5 Nov 2012; published 12 Nov 2012

such as 800 nm and 2 μm the behavior follows the same trend (see section 6.2). For instance, for a longer depth range of 2 μm, the crossing point is 50 photons/pixel. The loss of precision for DH-PSF in the high background regime is explained by the larger spread as compared to the astigmatic PSF, which leads to lower signal to background ratio. Note that these results are for the shot noise limited case only. For other noise sources like EMCCD gain noise, the results may vary but the general trend is preserved.

2.1 Analytic approach to Double-helix PSF generation

In order to attain an analytic expression for the DH-PSF phase mask we apply the properties of propagating vortices and the theory of rotating beams [28,29]. We further note that numerically generated designs typically and distinctively contain a set of vortices lying along a straight line [22]. Therefore, we propose to describe the pupil plane phase mask mathematically by a set of vortex singularities on a straight line along a diameter of the pupil. In radial coordinates, this phase function is generated by the following equation:

$$E_{pupil}\left(r,\theta\right) = circ\left(\frac{r}{R}\right)\exp\left(i\arg\left(\prod_{k=-M}^{M}\left(re^{i\theta} - r_k e^{i\theta_k}\right)\right)\right) \qquad (1)$$

where (r,θ) are the pupil plane co-ordinates, R is the radius of the pupil aperture, $M = (N\text{-}1)/2$, N is the number of vortices and (r_k,θ_k) is the location of the kth vortex. For DH-PSF-S, we used the CRB_{3D} metric and found the optimal number of vortices N to be 9 with the distance between successive vortices a constant $d = 0.66R$ (Fig. 1(b)). The phase mask has only three vortices located within the aperture while the other six are located outside but still have a significant effect on the phase in the aperture.

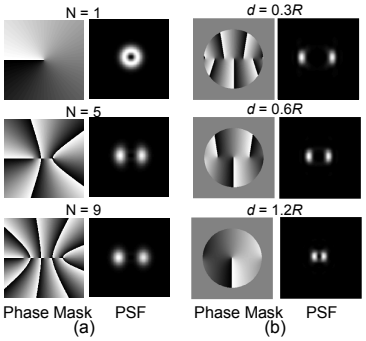

Fig. 2. Influence on the PSF of the number and distribution of vortex singularities in the pupil function. (a) The left column shows the pupil phase function (phase mask) with an increasing number of vortex singularities N and constant spacing d between them. The corresponding in-focus PSFs are shown in the right column. (b) Shows the change in the phase mask (left) and PSF at focus (right) as the spacing d increases with a constant $N = 9$.

Each vortex is a singularity of the phase so at its center the amplitude is zero, forcing the energy away from the center line and concentrating as two lobes on two opposite sides. In this design all the singularities have equal charge of + 1. Because the singularities have the same charge there is rotation of the field pattern in the far field [29]. The particular location of the singularities along a line generates two lobes and hence a double helix in 3D space. The relative location of the singularities (r_k,θ_k) and their number N is constant along the axial direction of the PSF.

Figure 2(a) shows the effect of increasing N, the number of vortex singularities, on the in-focus PSF. As N grows the diffracted energy is more confined in the two lobes of the PSF. On the other hand, Fig. 2(b) shows the effect of increasing the distance d among the vortex singularities. As d increases the two lobes of the PSF become closer, a direct result of the Fourier transform properties of wave propagation.

#173795 - $15.00 USD Received 6 Aug 2012; revised 16 Oct 2012; accepted 5 Nov 2012; published 12 Nov 2012

From a physical point of view the vortices are responsible for the rotating wave [29] effect exerted on the emission pattern from each single molecule. From an engineering point of view, helical PSFs of different pitch, Strehl ratio, and depth of field can be generated by modifying just two parameters: N and d/R. Therefore, varying the number and spacing of singularities provides two significant degrees of freedom that enable flexibility in the design of the DH-PSF. Moreover, if desired, a nonperiodic array of vortices provides additional design freedom. The new flexibility in DH-PSF design makes these microscope systems well suited for a variety of biological applications.

3. SPINDLE imaging - experimental details

The SPINDLE microscope setup shown in Fig. 3 was custom built on an optical table with the optical axis parallel to the table. Imaging was done with a 1.45NA 100X Nikon (Melville, NY, USA) objective using an electron multiplying charged coupled device (Andor EMCCD iXon DU897E CS0 #BV, South Windsor, CT, USA). The slide containing stained cells was mounted in a rose chamber which was locked down on a nano-positioning stage (Physike Intrumente PZ 164E, Irvine, CA, USA). The 488 nm line of Argon ion laser (Coherent, Santa Clara, CA, USA) was used for activation and the 641 nm diode laser (Coherent Cube) was used for deactivation. The lasers are combined with dichroic mirror-1 from Semrock (FF 541-SDi01-25x36, Rochester, NY, USA), to illuminate the sample uniformly with overlapping illumination. The lasers were used in synchronization with the EMCCD as shown in the acquisition/excitation scheme in Fig. 3. A digital pulse generator was used to control the 641 laser directly and 488 laser with a fast mechanical shutter (Uniblitz LS2 shutter, Vincent Associates, Rochester, NY, USA). Imaging was done at 20Hz with 1 activation pulse followed by 3 or 4 deactivation pulses from the 641 laser. Deactivation power density of 1-2 kW/cm^2 and activation power density of < 2 W/cm^2 was used. A polychroic mirror from Semrock (Di01-R405/488/561/635) was used to separate excitation and emission light. The emission was further filtered by two stacked dual-band filters (Semrock DBP FF01-538/685-25 and Omega XF3470 540-700DBEM, Brattleboro, VT, USA). The dual-band filters allow detection of emission of reporter dye Alexa-647 and the activator dye Alexa-488.

The DH-PSF was implemented by a 4F relay setup formed by two 100 mm focal length lenses (achromatic doublets, Edmund optics). The DH phase mask was placed at a plane conjugate to the pupil plane of the objective on an x-y-z translation stage. The DH mask was mounted on a magnetic kinematic mount to easily convert between a conventional and a DH-PSF microscope. The DH mask has a diameter of 2.7 mm and acts as the limiting aperture therefore reducing the effective NA of the system to 1.35. The mask was fabricated by the gray-scale lithography process described in Ref [30].

To estimate the 3D position from a molecule image a calibration is required. The calibration slide is mounted on the piezo translation stage and moved in axial direction through the focus while continuously acquiring images of the system PSF by imaging isolated single fluorescent beads. The stage is moved in 50 nm steps through the focus. Images of the PSF at various positions of the translation stage are shown in Fig. 4(a). The average images at each position are then given to a phase-retrieval algorithm which returns the complex fields at those positions to recover the 3D PSF [20]. The x-z and y-z plots for the recovered 3D PSF are shown in Fig. 4(b). These complex fields in each transverse plane are then used by the maximum likelihood position estimation algorithm.

#173795 - $15.00 USD Received 6 Aug 2012; revised 16 Oct 2012; accepted 5 Nov 2012; published 12 Nov 2012

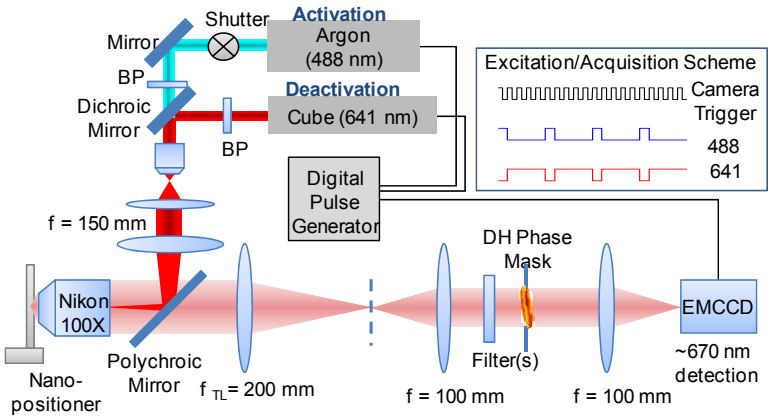

Fig. 3. Schematic of the SPINDLE microscope. The sample in the rose chamber is mounted on a piezo nanopositioner and imaged with a Nikon 1.45, 100X objective and 200 mm Nikon tube lens. The DH-PSF-S is implemented by a 4F relay setup formed by two 100 mm focal length lenses. The DH phase mask is placed at a plane conjugate to the pupil plane of the objective. The final image is formed on the EMCCD. The illumination lasers (641 nm Coherent Cube used for turn off and 488 nm Argon -ion for activation) are used in synchronization with the camera in the scheme shown on the top right.

The SPINDLE data is analyzed with a custom written MATLAB code to generate super-resolution images. Each image is analyzed to find potential molecule candidates and then position estimations done for those potential molecules. An example of the basic steps done in the process is shown in Fig. 4(c) and closely follows the method described in Ref [31]. The raw image is first smoothed with an average filter and then local peaks are found using appropriate parameters with non-maximum suppression [32]. The peaks above certain threshold of the background are selected and rough centers of the PSFs are found with peak positions of single lobes. The selected single molecule images are passed on to the 3D position estimator individually. We used maximum likelihood estimation (MLE) for position estimation which is based on phase-retrieval and is reported in Ref [20]. The maximum likelihood algorithm searches through the 3D PSF model to find the best match for the molecule image to determine its x, y and z position [20]. The noise process for the MLE was assumed to be Poisson. The axial position thus determined is corrected by a constant factor 0.79 which arises due to the refractive index mismatch between the coverslip and the mounting medium of the sample. The refractive index of the mounting medium was determined to be 1.35 whereas for the glass it is 1.515. As reported previously in Ref [9]. and [33] the axial magnification factor due to index mismatch can be assumed to be constant within a few micrometers of the coverslip.

We characterized the microscope by imaging and localizing a fluorescent bead in 3D as shown in Fig. 4(d). The precision value for each point in the curve is calculated with 1000 estimations for an in-focus PSF. We observed that the experimental precision did not vary significantly with axial position of the emitter over the range of operation. The estimation was done with the phase-retrieval based MLE, which is also used in the single molecule experiment described below. The theoretically calculated CRB is also reported for comparison in Fig. 4(d). The CRB calculation is performed with all the experimental parameters i.e. with PSF images generated from the measured DH mask, the EMCCD noise model (see section 6.7) with background of 1 photon/pixel, and NA1.35 100X, with detector pixel size of 16 μm at a wavelength of 670 nm. Note that the experiment follows closely the CRB, implying that the estimation algorithm is efficient. For instance, for 1100 photons the experimental precision is $(\sigma_x, \sigma_y, \sigma_z) = (21,20,51)$ nm and for 6000 photons the precision is $(\sigma_x, \sigma_y, \sigma_z) = (8,9,18)$.

#173795 - $15.00 USD Received 6 Aug 2012; revised 16 Oct 2012; accepted 5 Nov 2012; published 12 Nov 2012

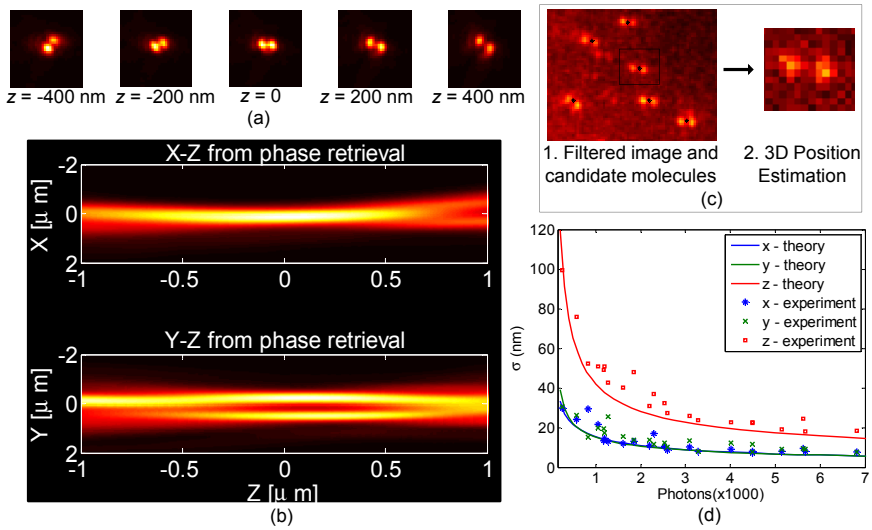

Fig. 4. Calibration and Phase Retrieval Interpolation: (a) Images of the 3D DH-PSF for various defocus positions. This data is taken with red beads (660/680 200 nm diameter from Invitrogen) fixed on cover slide and used as calibration for SPINDLE data analysis. (b) Result of phase retrieval to create continuous 3D PSF. This is used for maximum likelihood 3D position estimation of molecules. (c) Flowchart for processing of SPINDLE data. The image from the camera is filtered and potential molecule candidates are found (marked with black asteriks). Each candidate image is passed on to the estimator to find 3D position and number of detected photons. (d) Experimentally determined precision of a fluorescent bead compared with the CRB calculated for a 1 photon/pixel background under experimental conditions (see text).

4. 3D super-resolution imaging of microtubules with SPINDLE

We imaged microtubules of fixed PtK1 cells (Rat-kangaroo kidney epithelial cells) tagged with a tubulin antibody labeled with a pair of dyes acting as reporter and activator. A combination of Alexa-647 and Alexa-488 dyes was used as a photo-switch. Alexa-647 is the reporter dye of which the emission is detected and Alexa-488 is the activator to control the emission of the reporter. During the experiments no significant anisotropic effects were observed due to the rotational freedom of the dyes.

Figures 5(a)-5(d) show 3D super-resolution SPINDLE images of microtubules and a comparison with a normal wide field fluorescence image obtained using the same setup and high NA objective. In the super-resolution images, each localized single molecule is represented as a 2D Gaussian (scaled by the number of detected photons) and the colormap specifies the z dimension. The SPINDLE mask and experimental setup allow imaging over a depth of 1.2 μm.

From biological imaging point of view the SPINDLE images are different in three remarkable aspects: First, many of the details of the microtubule network are now clearly visible while they were missing in the normal fluorescence image. Second, the SPINDLE image provides three-dimensional information which is missing in normal fluorescence imaging. For instance, the crossing of two microtubules is easily resolved and determined to be 159 nm apart in the axial (z) direction, as shown in Figs. 5(e) and 5(f). Third, the SPINDLE image has a longer depth of field as illustrated by comparison of the upper left corners of Figs. 5(a) and 5(b).

We estimate the diameter of a single microtubule using a histogram of localizations in the transverse and axial dimensions as shown in Figs. 5(g) and 5(h), showing a FWHM of 80 nm in the transverse and 134 nm in the axial directions. These measurements are consistent with prior reports for the diameter for an antibody-stained microtubule of 60 nm [34] and the experimental resolution (FWHM) of SPINDLE.

#173795 - $15.00 USD Received 6 Aug 2012; revised 16 Oct 2012; accepted 5 Nov 2012; published 12 Nov 2012

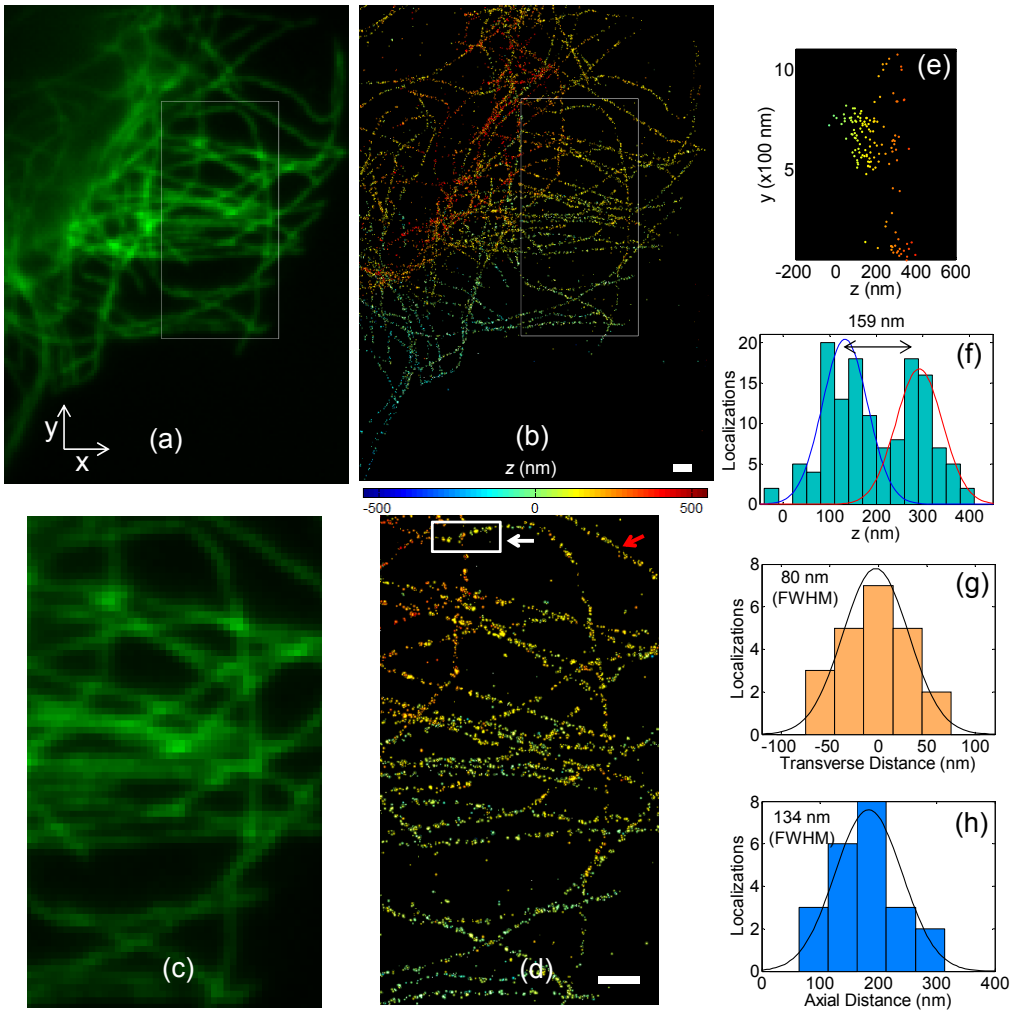

Fig. 5. (a) and (b) Comparison of classical fluorescence imaging and 3D SPINDLE imaging of tubulin of PtK1 cells (Rat Kangaroo Epithelial cells) using an antibody labeled with Alexa-647 and Alexa-488 dyes. (c) and (d) Zoomed in view of the boxed region in (a) and (b) to show details of microtubule structure. Colormap shows the *z* position. Scale bars are 1μm. (e) shows side-view of the boxed region in (d) and (f) shows a histogram of axial localizations to show separation of microtubules in *z* (Media 1 - the microtubules are shown in 3D from different views). (g) and (h) show transverse and axial cross-sections of the microtubule pointed with red arrow in (d) (Media 2 - the super-resolved microtubule is shown in 3D overlaid on the normal fluorescence image).

To establish the performance of SPINDLE experiment we performed precision analysis on molecule data from the same microtubule experiment mentioned above. Molecules which were emitting in consecutive images were identified as one molecule and their mean and standard deviation was calculated. Although we found that approximately 70% of the molecules turned off after one image, the remaining 30% stayed on up to 10 images. Out of these, the molecules which were on for at least 4 images were used for the precision analysis.

More details on the data analysis are provided in section 6.7. Figure 6(a) shows the calculated precision (standard deviation) with varying number of photons for each of the three dimensions. The error bars in the plot depend on the number of localizations used and the standard deviation value [35]. As expected, the precision increases with increasing number of photons. For comparison we also show the performance limit, √CRB, calculated for the same

#173795 - $15.00 USD Received 6 Aug 2012; revised 16 Oct 2012; accepted 5 Nov 2012; published 12 Nov 2012

experimental parameters (see section 6.7). It can be observed that for very low and high number of photons the estimated values approach the √CRB. For instance, for 1100 detected photons per image, the measured precisions are σ(x,y,z) = (22, 29, 52) nm, while the √Avg(CRB) values are σ(x,y,z) = (18, 23, 48) nm. Similarly for 5000 detected photons per image, the measured precisions are σ(x,y,z) = (7, 11, 22) nm, while the √Avg(CRB) values are σ(x,y,z) = (6.8, 7.5, 17) nm. Histograms of localization precision for 1100 and 5000 detected photons are shown in Figs. 6(b) and 6(c). The deviation in the estimated values from the √CRB can be attributed to over or under estimation of background value in the experiment and subsequent use in CRB calculation or the choice of the noise statistics affecting the estimator performance. The background value used here is the median value of 30 photons/pixel but it varied from 20 to 60 photons for the entire set. For the estimator, the noise distribution was assumed to be Poisson. Improvements in the estimator to incorporate the noise distribution of the EMCCD camera could further improve the current precision values. The resolution values of (Δx,Δy,Δz) = (6,9,39) nm FWHM with 6000 photons per image is already an improvement over prior STORM experiments [9] while offering at least a 50% longer depth of field [9,11].

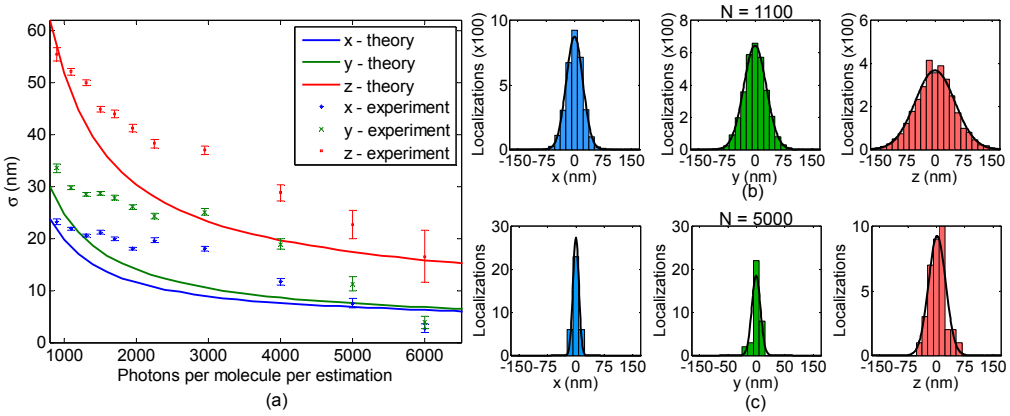

Fig. 6. Precision analysis of the SPINDLE data. (a) Precisions per localization in *x*, *y* and *z* directions for different number of photons per image. Theoretical √CRB values calculated for the same system parameters with 30 background photons/pixel and the probability density function for the EMCCD are shown for comparison with the experiment. The theoretical values correspond to √Avg(CRB) for 1.2 μm range. (b) and (c) Histograms of *x*, *y* and *z* estimated positions for molecules detected with 1100 photons and 5000 photons per image, respectively. The measured precision values for (b) and (c) are σ(x,y,z) = (22,29,52) nm and σ(x,y,z) = (7,11,22) nm.

5. Conclusions

The SPINDLE experiment demonstrates a 3D super-resolution system based on the DH-PSF as a flexible tool for biological imaging revealing details of structures at the nano-scale level. The SPINDLE method incorporates the advantage of a Fisher information optimized DH-PSF design, a photo-efficient PSF implementation with a polarization insensitive phase mask, and an optimal 3D position estimator to achieve long depth range super-resolution imaging with high precision. Further, the proposed analytic design approach provides insights into the influence of parameters such as number of vortices and distribution in the performance of helical PSFs. The new DH-PSF-S design improves performance in high background with a minor compromise in the depth range. It also demonstrates the inherent flexibility of PSF engineering to choose a DH-PSF based on the specific application requirement. For instance, specific DH-PSF designs can target long or short depth range or a low or high background noise environment. The surface relief phase mask increases the efficiency, ease and flexibility of use over the SLM based systems [30]. Furthermore, the phase retrieval based MLE for 3D

#173795 - $15.00 USD Received 6 Aug 2012; revised 16 Oct 2012; accepted 5 Nov 2012; published 12 Nov 2012

localization increases the precision over the widely used Centroid and Gaussian estimators [20].

With the combination of these capabilities SPINDLE shows super-resolution imaging of micro-tubules with photo-switchable red dyes like Alexa-647 even with low photon counts. Hence, photo-activatable proteins with lower quantum efficiency can also be used with SPINDLE [18]. Photo-switchable probes are also attractive for multi-color imaging with single wavelength detection making use of a single phase mask in the SPINDLE microscope [34].

6. Appendix

6.1 PSF calculation

The PSF images shown in Figs. 1 and 2 are calculated using the scalar paraxial model from their respective pupil functions. For high NA objectives and for isotropic emitters like fluorescent beads and randomly rotating dipoles the scalar paraxial model has been found to be a good approximation [36]. For the incoherent PSF in microscopy the transfer function is the pupil function of the microscope. Since we insert DH-PSF mask in the pupil plane (experimentally re-image the DH-PSF phase mask onto it), the DH-PSF phase mask is the transfer function. The 2D PSF images at different defocus positions of a microscope are computed by multiplying the transfer function by a quadratic phase factor, calculating the inverse Fourier transform, and then its modulo-squared value, given by:

$$PSF\left(x,y,z\right)=\left|\Im^{-1}\left\{H\left(u,v\right)\exp\left[-i\frac{\pi}{\lambda n_{oil}}NA^{2}dz\left(u^{2}+v^{2}\right)\right]\right\}\right|^{2} \qquad (2)$$

where (u,v) are normalized pupil plane co-ordinates and $H(u,v)$ is the pupil function, NA is the numerical aperture of the objective, n_{oil} is the refractive index of the oil and dz is the defocus distance and $\Im$ is the 2D Fourier transform operator.

6.2 CRB comparison of different PSFs

Figures 7(a) and 7(b) show a comparison of the average 3D CRB for the different localization methods. Here the axial range is 800 nm and 2 μm showing the behavior is consistent with Fig. 1(e). The DH-PSF-S provides the lowest CRB for experiments with background photons up to 40 - 50 photons/pixel.

Figure 7(c) shows the CRB as a function of x, y and z directions with varying axial position of the emitter. CRB_{3D} is the average of CRB for x, y and z. It is seen that the CRB for transverse dimensions are relatively flat as compared to the axial CRB. It is important to achieve a flat and uniform CRB_z over the entire depth but we have observed that some loss of flatness is required to achieve a lower CRB by concentrating more energy in the two lobes [18,19]. We have optimized the DH-PSFs by keeping a low variation in CRB_z while still achieving a low CRB_{3D}.

6.3 Labeling of PtK1 cells with photoswitching probes

PtK1 cells were seeded onto glass coverslips and fixed when they reached ~70% confluency. Cells were rinsed rapidly with 37°C 1X PHEM buffer (60mM PIPES, 25mM HEPES, 10mM EGTA, 4mM MgSO4, pH 7.0) followed by lysis at 37°C for 5 min in freshly prepared lysis buffer (1X PHEM + 0.5% Triton-X-100). Cells were then fixed on the bench top for 3 min using ice cold methanol (95% methanol + 5mM EGTA) followed by an additional 20 min methanol fixation at −20°C. At room temperature, cells were then rehydrated with 1X PHEM then rinsed 3X5 min in PHEM-T (1X PHEM + 0.1% Triton-X-100) and blocked in 10% boiled donkey serum (BDS) in PHEM for 1 hr at room temperature. Microtubules were labeled with anti-alpha tubulin primary antibodies (Sigma-Aldrich, St. Louis, MO) diluted in

#173795 - $15.00 USD Received 6 Aug 2012; revised 16 Oct 2012; accepted 5 Nov 2012; published 12 Nov 2012

5% BDS for 12 hr at 4°C. Following primary antibody incubation, cells were rinsed 3X5 min in PHEM-T and then incubated for 45 min at room temperature with secondary antibodies. Secondary antibodies were double labeled with activator/reporter pairs according to the methods described in Bates et al [34]. Briefly, Alexa 647 and Alexa 488 (Invitrogen, Grand Island, NY) were conjugated onto secondary IgG antibodies with a stoichiometry of ~2 Alexa 488 / 0.6 Alexa 647 molecules per antibody. Cells were then rinsed 3X5 min in PHEM-T and post fixed at room temperature for 10 min using freshly prepared 1% paraformaldehyde (Ted Pella Inc., Redding CA). Following post-fixation, cells were rinsed 3X5 min in PHEM-T and then stored in PHEM until imaging. Cells were mounted in Rose Chambers and immediately before filming, the chamber was filled with imaging buffer (50mM TRIS-HCl pH 8.8, 10mM NaCl, 10% glucose, 0.56mg/mL glucose oxidase (Sigma), 600µg/mL catalase (Roche Applied Science) and 100mM cysteamine (Sigma)).

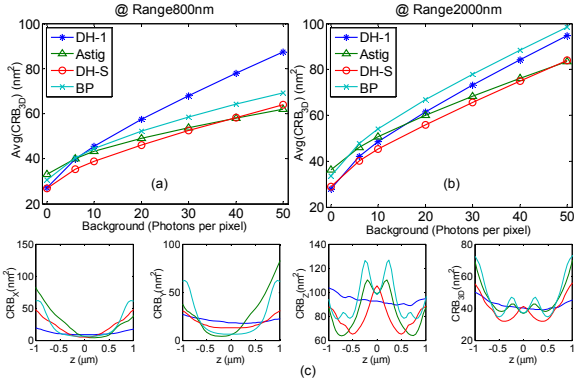

Fig. 7. (a)-(b) Comparison of 3D localization methods via the Average Cramer Rao Bound (CRB_{3D}) over 800 nm and 2 µm ranges with changing background. The calculation parameters for shot-noise limited CRB are 1.45NA, λ = 660 nm, pixel size = 16 µm, 3000 detected photons at focus. (c) shows the CRB for each dimension (*x*,*y* and *z*) and the 3D CRB varying with *z* for background of 6 photons/pixel.

6.4 Fiduciary beads on cell slides

Fiduciary beads, 40 nm in diameter (660/680, Invitrogen), were applied to coverslips prior to the addition of cells. To 100 µL of 1X PBS, 1.5µl of fiduciary marker suspension was added, and of this suspension, 100µL was added to the coverslips and incubated for 4 hr at room temperature. Coverslips were washed once with 1X PBS, cells were added directly to these coverslips, grown to confluency, and then processed as described above.

Fiduciary beads were used for monitoring drift in the SPINDLE experiment and for drift correction in post analysis of the data. The fiduciary bead was also used to keep the setup roughly in focus manually from time to time. About 1-2 beads were used for drift correction in each data analysis.

6.5 Calibration beads

For 3D position estimation with DH-PSF microscopy, a calibration has to be done. This is usually done right before or after the experiment. The calibration slide was prepared by making a dilution of bright beads (660/680 200 nm diameter from Invitrogen) in pure water and putting on the coverslip. The beads are allowed to dry for a few hours and the coverslip is washed twice with pure water. The coverslip is then stuck on the glass slide with imaging buffer filled in between them.

6.6 Camera calibration

For accurate calculation of the number of detected photons, the conversion factor *m* between photons and camera counts was determined. The obtained count value for each pixel is

#173795 - $15.00 USD Received 6 Aug 2012; revised 16 Oct 2012; accepted 5 Nov 2012; published 12 Nov 2012

divided by m to determine the number of photons. This was done by two methods which gave the same value for m. The experimental setup for both methods was the same which was to put a diffused light source in front of the objective to capture a uniform illumination on the camera. The light source is then turned off and camera shutter closed to capture dark/offset value with EM gain on and EM gain off.

The first method determines the camera electron multiplication (EM) gain and the analog to digital (A/D) gain separately. The A/D gain was determined to be 10.69 for our camera settings by the method mentioned in [37]. The EM gain was found to be 300 (the same as software setting) by capturing the signal with EM gain on and EM gain off. The ratio of the ($Signal_{EMon}$-$Dark_{EMon}$)/($Signal_{EMoff}$-$Dark_{EMoff}$) then gives the EM gain value. So the conversion value from counts to photons was m = 300/10.69 = 28 counts/photons.

The second method to determine the conversion factor is to determine the conversion statistics for the camera and obtaining the parameters. In Refs [38]. and [39], it has been shown that for an electron-multiplying CCDs such as the Andor iXon DV-897-BV used here, the probability density function for the camera counts c is given by

$$G_{p,m}(c) = e^{-p}\delta(c) + \sqrt{\frac{p}{cm}}e^{-\frac{c}{m}-p}\,BesselI_1\left(2\sqrt{\frac{cp}{m}}\right) \qquad (3)$$

where p is the number of photons hitting the pixel, m is the camera conversion factor (counts/photons) and $BesselI_1$ is the first order modified Bessel function of first kind. Uniform illumination images were acquired and offset corrected to plot the distribution of pixel values as shown in Fig. 8. By fitting the histogram with the probability distribution functions in Eq. (3), value of conversion factor m was obtained to be 27.4 counts/photons. The value of m is approximately the same for a camera with given settings independent of the illumination.

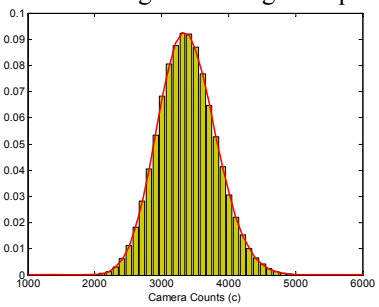

Fig. 8. Determination of noise in the experiment. The histogram of pixel values was obtained by taking 200 frames and 200x200 window size. The histogram was fitted with the given EMCCD probability distribution. From this fitting, the parameter values obtained are m = 27.5 camera counts per photons and p = 123 photons.

6.7 Precision analysis and experimental CRB calculation

To calculate the precision of position estimation in the microtubule experiment reported in the main text, molecules ON/emitting in consecutive images were identified and their weighted mean calculated. Molecule positions which were within 200 nm of each in transverse dimensions in consecutive images were identified as single molecules. For 30,000 frames collected, total estimations were 121,715. We observed that majority of emitters turned off after one image. The histogram in Fig. 9(a) shows the percentage of emitters ON for different number of images. Since ~70% of molecules were ON for single image experimental precision of these could not be calculated. But we found that distribution of number of collected photons across these single image emitters was same as those which were ON for 4 or more images. Figures 9(b) and 9(c) show histograms of photons collected for molecules which were ON for single image and molecules which were on for 4 or more images, respectively. Hence, we can use the molecules which were ON for 4 or more images to

#173795 - $15.00 USD Received 6 Aug 2012; revised 16 Oct 2012; accepted 5 Nov 2012; published 12 Nov 2012

represent the precision for the entire data set. For calculating precision values for a given number of photons reported in Fig. 6, molecules within N ± ΔN/2 were selected.

Calculation of the theoretical precision in Figs. 4(d) and 6(a), for *x*, *y* and *z* positions with varying number of photons was done by assuming the probability distribution function in Eq. (2) and experimentally determined value of *m*. The σ values in Fig. 6 are √Avg(CRB) for 1.2 μm range around focus. The CRB calculation was done by method explained in Ref [40]. for NA 1.35 100X with detector pixel size of 16 μm at the wavelength of 670 nm. The DH-PSF images used for CRB calculation was simulated with the profilometer measurement of the phase relief mask. The background photon value was estimated for each molecule by method described in Ref [20]. The median value of 30 photons/pixel was used for CRB calculation in Fig. 6(a).

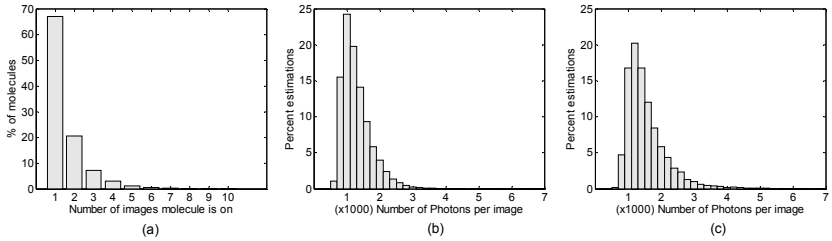

Fig. 9. Statistical analysis of molecules with respect to number of cycles ON. (a) Histogram of molecules based on number of images they were ON in a SPINDLE experiment. Total number of estimations using 30,000 frames was 121715. The majority of molecules are ON for a single image. (b) Distribution of 55481 estimations which were found to be ON for a single image with the number of photons per image. (c) Distribution with number of photons per image for 20820 estimations, each of which was found to be related to molecules ON four or more images in the experiment. The two distributions are similar showing that precision values (in Fig. 6) calculated from molecules which were ON for 4 or more images can be used for the entire data set, including the molecules which were ON for a single image.

Figure 10 shows a classical fluorescence and super-resolution image of another microtubule region acquired with SPINDLE microscope. 1 μm depth of the region is shown in colormap of the super-resolution image.

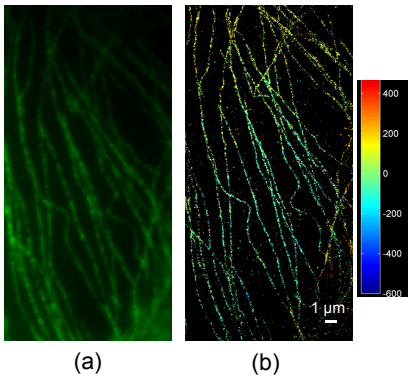

Fig. 10. (a) Normal fluorescence image of microtubules region and (b) 3D SPINDLE image of the same region. The depth is shown in colormap.

Acknowledgments

This work was supported by NSF awards DBI-0852885, DBI-1063407, and DGE-0801680. J.G.D. is supported by a PEW Scholars Award in the Biomedical Sciences. We thank Dr. Bo Huang for helpful discussions. We would like to thank the Colorado Nanofabrication Laboratory at the University of Colorado Boulder for using their facilities to fabricate the surface relief phase mask

#173795 - $15.00 USD Received 6 Aug 2012; revised 16 Oct 2012; accepted 5 Nov 2012; published 12 Nov 2012